Materials Characterization 166 (2020) 110406

Contents lists available at ScienceDirect

Materials Characterization

journal homepage: www.elsevier.com/locate/matchar

Non-acid, alcohol-based electropolishing enables high-quality electron backscatter diffraction characterization of titanium and its alloys: Application to pure Ti and Ti-6Al-4V

Nicholas C. Ferreri, Daniel J. Savage, Marko Knezevic*

Department of Mechanical Engineering, University of New Hampshire, Durham, NH 03824, USA

ARTICLE INFO

Keywords:
Electropolishing
EBSD
Titanium
Ti-6Al-4V
Microstructure
Twinning

ABSTRACT

This paper conceives an electropolishing sample preparation procedure aimed at characterization of titanium (Ti) and its alloys using electron backscatter diffraction (EBSD). Specifically, it is shown that a single non-acid, ethanol-ethylene glycol-NaCl electrolyte solution can be used to electropolish Ti and its alloys for obtaining high-quality EBSD datasets. As a result, the use of hazardous acids common in standard Ti metallographic preparation procedures, such as hydrofluoric, perchloric, and sulfuric acid, can be circumvented. Moreover, electropolishing Ti with an ethanol-ethylene glycol-NaCl electrolyte is performed at room temperature with low voltage, as opposed to the low temperatures and/or high voltages used when electropolishing Ti in traditional solutions. The utility of the novel procedure is demonstrated on samples of pure α-Ti before and after plastic deformation and on samples of alloy Ti-6Al-4V created by additive manufacturing (AM) in stress-relived and heat-treated conditions. EBSD scans performed on undeformed pure α-Ti had high-quality diffraction patterns, which allowed for large areas to be scanned at fast speeds without sacrificing indexing accuracy. The electropolishing created excellent surfaces on the deformed pure α-Ti sample despite elevated lattice strains and numerous deformation twins in its microstructure. It also allowed for detailed EBSD mapping of fine sub-grain features in AM Ti-6Al-4V despite the alloying additions of aluminum and vanadium, the inhomogeneous AM microstructure, and the different processing conditions. It is anticipated that the major breakthrough achieved in this work will streamline and make safer future metallographic studies of Ti and its alloys.

1. Introduction

Titanium (Ti) is a transition metal that in its metallic form has a range of desirable mechanical and chemical properties that make it a structural material in high demand [1–3]. Ti has a high specific strength, melting point (1688 °C), biocompatibility, and corrosion resistance in oxidizing environments [1,4–8]. Metallic Ti has three equilibrium phases: a hexagonal close-packed (hcp) phase (α-Ti), a body-centered cubic (bcc) phase (β-Ti), and a hexagonal phase (ω-Ti). Through the use of alloying and heat-treating, major alterations can be made to Ti microstructures, which can be tailored to alter and enhance specific material properties. This flexibility has led Ti and many of its alloys, such as Ti-6Al-4V, to become excellent structural materials, particularly in aerospace, marine, and medical industries [9–12].

During the research and development of Ti alloys, comprehensive microstructural analysis is performed to study the relationship between observed structure and material properties. Throughout this process, metal samples can be examined by various characterization techniques. Depending on these techniques, specific surface finishes are required to reveal specific microstructural features. To achieve proper surface quality, samples are prepared metallographically. Often, samples are ground with silicon carbide (SiC) or alumina (Al_2O_3) abrasive paper, followed by a fine polish using an alumina, silica (SiO_2), or diamond suspension on a non-abrasive pad [13,14]. Chemical etchants or acidic/alkaline polishing suspensions can also be used as a final step to reveal certain microstructural features or when a specific material responds better to chemical dissolution versus mechanical removal [13].

Ti is a difficult material to mechanically polish, which makes it difficult to achieve pristine surface finishes for certain scanning electron microscope (SEM) techniques such as electron backscatter diffraction (EBSD) [13]. Therefore, when preparing Ti for EBSD, samples are often etched with a solution that utilizes a strong and/or oxidizing

* Corresponding author at: University of New Hampshire, Department of Mechanical Engineering, 33 Academic Way, Kingsbury Hall, W119, Durham, NH 03824, USA.
E-mail address: marko.knezevic@unh.edu (M. Knezevic).

https://doi.org/10.1016/j.matchar.2020.110406
Received 2 February 2020; Received in revised form 26 April 2020; Accepted 26 May 2020
Available online 28 May 2020
1044-5803/

acid such as hydrofluoric acid (HF), perchloric acid ($HClO_4$), or sulfuric acid (H_2SO_4) [13,15–18]. Another method of surface treatment common with Ti is electropolishing. Electropolishing can be favorable over etching because of its conformability, speed, and ability to remove large amounts of material autonomously [19,20]. That being said, for Ti, the electrolyte solutions include combinations of the previously mentioned acids, which are particularly toxic and generally require the use of high voltages and variable working temperatures in order to be effective [20,21]. Fushimi et al. [22,23] investigated the electropolishing of commercially pure (CP) Ti at room temperature in a 1 M ethylene glycol ($C_2H_6O_2$)-sodium chloride (NaCl) electrolyte solution. Furthermore, Kim et al. [20] expanded on this methodology and investigated the effect of ethanol (C_2H_6O) additions on the anodic dissolution of Ti in a 1 M ethylene glycol-NaCl solution. It was determined that 20% ethanol by volume in solution produced the best surface finish (2.341 nm), with no noticeable sign of surface oxides [20].

The purpose of this study was to adopt the electropolishing technique explored in Kim et al. [20] to undeformed, ultra-high purity (UHP) α-Ti and semi-quantitatively test its effectiveness as an EBSD preparation by observing the fraction of EBSD patterns indexed with a confidence index (CI) $>$ 0.10 as a function of bin size and imaging gain. Furthermore, samples of deformed UHP α-Ti and an additively manufactured (AM) Ti-6Al-4V alloy with two different processing histories were subsequently electropolished and scanned to test the effectiveness of the ethanol-ethylene glycol-NaCl electrolyte solution on pure, alloyed, undeformed, deformed, and heat-treated Ti with regard to EBSD preparation. The collection of high quality UHP α-Ti and Ti-6Al-4V EBSD datasets, made possible via electrolytic surface preparation with a single non-acid, electrolyte solution using low voltage at room temperature, would eliminate the need for HF, $HClO_4$, H_2SO_4, and/or low temperature solutions. The methods presented here eliminate the hazards of working with such acids and provide highly polished surfaces for electron microscopy with a simple apparatus.

2. Material preparation

2.1. Sample fabrication

The samples originating from a hot-rolled plate of UHP α-Ti supplied by Fine Metals Corporation had an elemental composition of 99.9993 at.% Ti, which was determined via glow discharge mass spectroscopy (GDMS). A LECO combustion infrared detection technique was used to separately measure the concentrations of elements with low atomic number. These elements, with smaller metallic radii, can have substantial influence on deformation mechanisms in hcp materials because they occupy interstitial lattice sites and create anisotropic strain fields that could alter either *a* or *c* lattice parameters [24]. The interstitial elements detected were oxygen, carbon, and hydrogen and had respective concentrations of 219, 12.5 and 1 ppm.

To manufacture cylinders of UHP α-Ti for compression testing, oversized blocks of material were cut from the plate and heat-treated in a sealed Lindberg/Blue tube furnace under UHP argon (Ar) with a flow rate of 2 L/min at 800 °C. After soaking at temperature for 2 h, the heating element in the furnace was turned off and the blocks were cooled under equilibrium conditions to room temperature. Cylinders were machined from these blocks such that their surfaces were all $>$ 1 mm from the free surfaces of the blocks. This was done to prevent samples from having grains that may have been damaged or plastically deformed while the plate was being processed and to remove smaller grains that were pinned to free surfaces when grains coarsened during heat-treating [25]. 6 samples were machined so that their loading axes are along the plate's rolling direction (RD). This can be seen in Fig. 1 where the cylinders are shown with respect to the processing frame and the blocks they were cut from. For these RD samples, oversized bars of material were turned on a lathe to create elongated cylinders from which the smaller cylindrical samples were cut. Final compression samples had heights of 8.0 mm and diameters of 6.3 mm per ASTM E9 standards [26,27]. The described sample manufacturing and processing procedure for UHP α-Ti was implemented because these samples were used in a study by Savage et al. [28] where Ti deformation mechanisms were observed during compression as a sole function of initial grain size. In the present work, only 2 of the 6 compression samples were used: one to observe the microstructure of undeformed UHP α-Ti and one that was compressed to observe the microstructure of deformed UHP α-Ti.

Bulk cylindrical specimens were built from Ti-6Al-4V gas atomized powder (3D Systems, Rock Hill, SC) on a 3D Systems model ProX300 metal powder bed fusion (PBF) additive manufacturing system in an argon atmosphere. Processing parameters were as follows: laser power = 275 W, laser speed = 1800 mm/s, hatch spacing = 85 μm, and layer thickness = 40 μm. Parts were stress relieved while still attached to the build platform using a thermal cycle of 4 h at a temperature of 600 °C in an argon atmosphere. Following the stress relief treatment, the samples were electric discharge machined from the build platforms. A set of low-cycle fatigue (LCF) specimens were turned on a lathe to have $>$ 1 mm of material removed from all free surfaces. These specimens were machined according to ASTM E606 specification [29,30].

A set of these samples were then removed from the build platform prior to machining and underwent a Thermo-hydrogen Refinement of Microstructure (THRM) [31] treatment, which aimed to create samples with an alternate initial microstructure. This process is largely based on a powder metallurgy process called Hydrogen Sintering and Phase Transformation (HSPT). However, whereas the HSPT process is meant to produce bulk components from powder compacts, THRM has been developed as a post-process for bulk Ti products produced by virtually any means. The key innovation of THRM is the ability to heal defects (e.g. pores and cracks) and produce wrought-like microstructures from essentially any material starting condition through hydrogen-enabled mechanisms. Defects are healed due to enhanced Ti self-diffusion produced by the presence of relatively weak Ti—H bonds, which is driven by the surface energy associated with pores and cracks. As such, many defects are healed without requiring applied pressure. Furthermore, and perhaps more importantly, THRM can produce a range of wrought-like microstructures. Like the stress-relieved material, LCF specimens were also machined from the THRM-treated material. The described sample manufacturing and processing for Ti-6Al-4V was implemented because these LCF specimens were used in a study by Ghorbanpour et al. [32] to observe the effect of THRM on fatigue life in AM Ti-6Al-4V. In this work, cross-sectional slices (Fig. 1(b)) from the grip sections of a stress-relieved and THRM-treated LCF sample were characterized by EBSD.

2.2. Alcohol-based electropolishing

Prior to characterization, both undeformed and deformed compression cylinders were electropolished to remove microscopic surface roughness and ensure high-contrast EBSD images. Samples were first prepared by grinding using 120, 180, 240, 320, 400, and 600 grit SiC abrasive. This created a uniform surface on both faces of the cylinder, which improved reactivity and ensured a homogeneous distribution of charge across sample surfaces by removing oxides that may have formed during processing [20].

A schematic of the electropolishing setup is shown in Fig. 2 with labels identifying components of the electrochemical cell. The cell's housing is a standard 250 mL Pyrex beaker and within are two electrodes, the electrolyte solution, and a 40 mm long Teflon-coated, Azlon Oval magnetic stir bar. The electrodes were made from a 304-grade stainless steel (304-SS) sheet that was cut into 30 mm × 100 mm × 2.0 mm strips. The cathode was covered with a napped polypropylene fabric, supplied by Allied Plating, to provide nucleation sites for dissolved hydrogen gas (H_2), which accelerated H_2

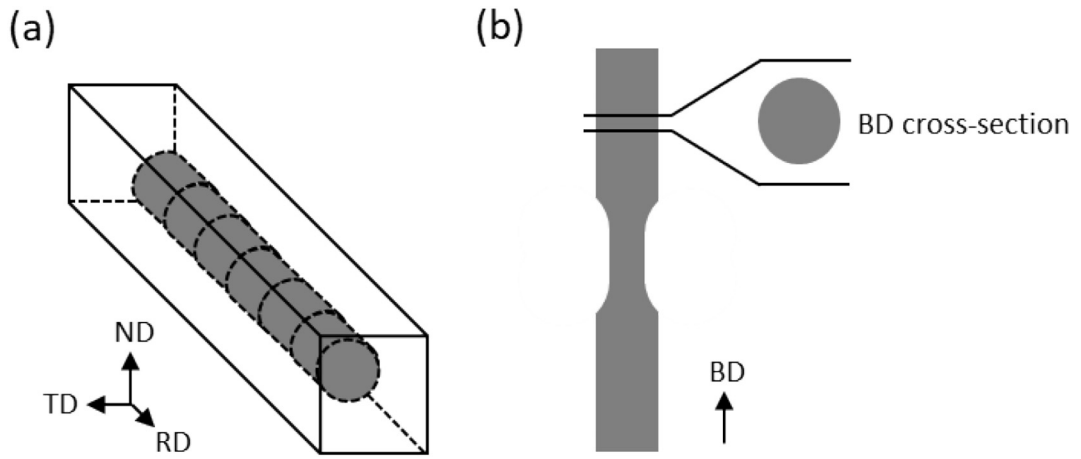

Fig. 1. UHP α-Ti compression cylinders (a) were machined from oversized blocks of material, which were cut from the original hot-rolled plate so that their loading axes were along the plate's rolling direction (RD). Other axes in the UHP α-Ti sample frame are the direction transverse to rolling (TD) and normal to rolling (ND). Both stress-relieved and THRM-treated Ti-6Al-4V samples were sectioned from the grip regions of respective fatigue specimens (b) that had their length aligned with the build direction (BD) of the AM processing frame.

removal from the system, increasing surface finish quality [20]. The anode was made by adhering the Ti sample to the 304-SS strip via a general-purpose not conductive stop-off lacquer (Tolber Chemical Division). The lacquer was applied so that the entire height of the sample was coated. Vinyl electroplaters tape was used to seal the upper portion of the anode, while the lacquer was used again to cover the lower portion. This left only the one face of the Ti cylinder exposed to the electrolyte solution. When inserted into the electrolyte solution, the electrodes were stabilized by a polycarbonate electrode mount and kept parallel to one another at a 20 mm working distance. Lastly, a TENMA 72–6628 was used to supply direct current (DC) to the system, and a VWR 325 hotplate/stirrer was used to rotate the stir bar within the

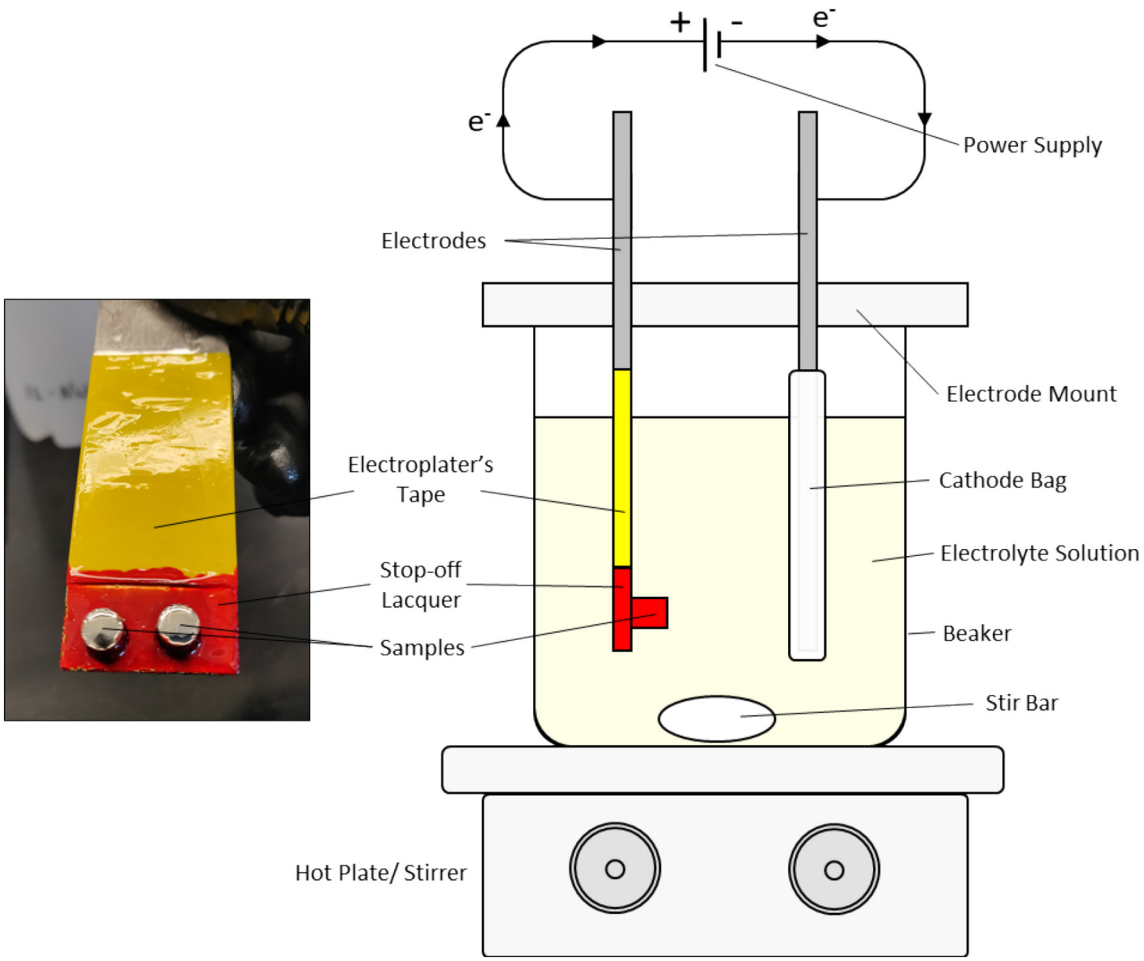

Fig. 2. Labeled schematic of experimental setup used for electropolishing Ti cylinders in an ethanol-ethylene glycol-NaCl electrolyte solution (right). An image of two compression cylinders fixed to the working electrode after having been electropolished is also shown (left).

solution.

To create the electrolyte solution, 58.44 g of powdered NaCl (Fischer Chemical) was dissolved into 99.0% ethylene glycol (Beantown Chemical) to create 1 L of 1 M NaCl solution. Because ethylene glycol is not as polar of a molecule as other solvents like water [33], the dissolution is time consuming; but the process can be accelerated by slightly heating the mixture (~75 °C) and stirring with a magnetic stir bar. Once dissolved and prior to electropolishing, 200 proof ethanol (Greenfield Global) was added to create a solution of 20% by volume ethanol. Specifically, 40 mL of ethanol was mixed with 160 mL of the ethylene glycol-NaCl solution in the electrochemical cell just prior to electropolishing to minimize moisture absorption and ethanol evaporation [34,35].

A linear sweep voltammetry experiment was performed on a Ti sample to determine the proper potential to apply when electropolishing. Current (I) was measured while the potential (V) applied between the two electrodes was swept linearly in time. All I measurements were normalized by the total area of the anode exposed to the electrolyte solution and plotted against the corresponding applied voltages. This relationship between current density (J) and electrochemical potential is shown in Fig. 3 and describes the anodic polarization behavior of UHP α-Ti and Ti-6Al-4V. Anodic polarization curves have three distinct regions: An initial stage showing a rapid increase in J with increasing potential, a plateau region where J increases slowly (highlighted in Fig. 3), followed by a third region at higher potentials where J increases rapidly again.

Anodic dissolution begins during the initial stage, represented by Eq. (1), and after continuing to increase the energy in the system, eventually a steady state is reached whereby a passive Ti tetrachloride ($TiCl_4$) film forms on the Ti surface, represented by Eq. (2) [20]. The mass-transfer-limited rate of dissolution occurs in the plateau region due to the formation of the stable $TiCl_4$ film and therefore represents the optimal range of potentials for electropolishing [36]. It is within this range where material removal is most even and constant. When increasing potential past the saddle region, there can be severe oxygen gas (O_2) evolution and widespread pitting on the substrate surface

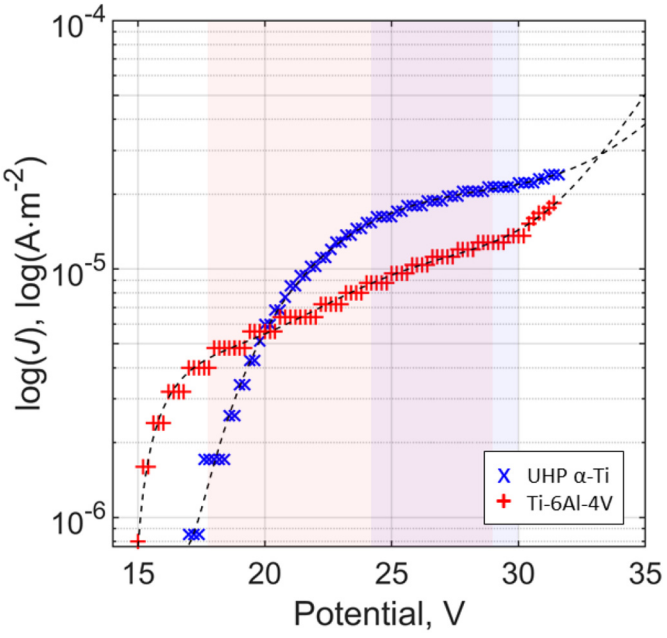

Fig. 3. Anodic polarization curves for the electrochemical reaction of UHP α-Ti and Ti-6Al-4V in an ethanol-ethylene glycol-NaCl electrolyte solution. The red and blue shaded zones highlight saddle regions on the UHP α-Ti and Ti-6Al-4V plots, respectively, which indicate ranges of favorable electropolishing potentials. (For interpretation of the references to color in this figure legend, the reader is referred to the web version of this article.)

[36,37]. This was confirmed for UHP α-Ti as we observed excessive O_2 production, which produced small, uniformly distributed pitting (< 10 μm in diameter) when applying potentials greater than ~30 V (~29 V for Ti-6Al-4V). For UHP α-Ti, when applying potentials less than ~24 V (~18 V for Ti-6Al-4V), we saw inhomogeneous surfaces with a combination of polished and unpolished areas as well as other areas with large pits likely created from unevenly distributed $TiCl_4$ film:

$$Ti \rightarrow Ti^{4+} + 4e^- \quad (1)$$

$$Ti^{4+} + 4Cl^- \rightarrow TiCl_4(l) \quad (2)$$

The $TiCl_4$ film can also be detrimental to the anodic dissolution of Ti by passivating the substrate surface if not removed. $TiCl_4$ is a viscous liquid and to facilitate its removal from the electrode, there needs to be strong stirring forces within the electrochemical cell [20]. When stirring at an rpm < ~150, we observed surface passivation due to the lack of $TiCl_4$ film dissolution, and when using an rpm > ~350 we observed inhomogeneous surfaces with regions of both pitting and polishing. We believe a high rpm dissolves the $TiCl_4$ film too quickly in regions, which promotes the uneven polishing and localized pitting. The film's dissolution is described in Eqs. (3) and (4) whereby the ethanol (EtOH) helps dissociate the $TiCl_4$ into protons (H^+), chlorine ions (Cl^-), and Ti ethoxide (Ti $(EtO)_4$). The Ti $(EtO)_4$ can then also break down further into titania (TiO_2) and ethanol:

$$TiCl_4 + EtOH \rightarrow Ti(EtO)_4(l) + 4H^+ + 4Cl^- \quad (3)$$

$$Ti(EtO)_4(l) + 2H_2O \rightarrow TiO_2(s) + 4EtOH \quad (4)$$

It was determined that the applied potentials and stirring rates that provided the best surfaces (flat, no oxide layer, and no pitting) were 27.5 V and 300 rpm for the UHP α-Ti cylinders (deformed and undeformed) and 25.0 V and 300 rpm for the Ti-6Al-4V samples (stress-relieved and THRM-treated). All samples were electropolished in room temperature solution (23 °C) for 50 min at a constant applied potential. When using these parameters and performing consecutive electropolishing experiments, it was found that surface and EBSD pattern quality did not noticeably degrade as the electrolyte solution was reused up to three times.

3. Characterization and testing

3.1. Monotonic compression

In order to prepare a sample of deformed UHP Ti for the study, compression testing was performed on a servohydraulic INSTRON 1350 with a 100 kN load cell and DAX software and controller. The utilized INSTRON machine is equipped with a customized compression fixture that contains two cylindrical compression dies vertically aligned along the actuator axis [38–42]. The two dies are mounted on separate crossbeams connected by linear guides, which ensures parallel translation parallel with respect to one another. Prior to experimentation, samples and compression dies, made of hardened steel with smoothly ground flat surfaces, were lubricated with colloidal graphite. The compression test was conducted at room temperature, actuator displacement and load were recorded at a frequency of 20 Hz, and a strain rate of 10^{-3} s^{-1} was maintained throughout all tests. The UHP α-Ti cylinder was compressed along RD to a true strain of 0.2.

3.2. EBSD optimization

Both undeformed and deformed samples were electropolished prior to characterization. Once electrolytically prepared, they were adhered to aluminum stubs via carbon paint, fixed to a 70°, pre-tilted mount, inserted into a TESCAN LYRA 3 GMU SEM and scanned with an accelerating voltage of 20 kV. Incident electron beam spot diameters were fixed at 150 nm for all samples, and working distance were maintained at ~9 mm. A HIKARI XP2 detector was used to collect EBSD patterns

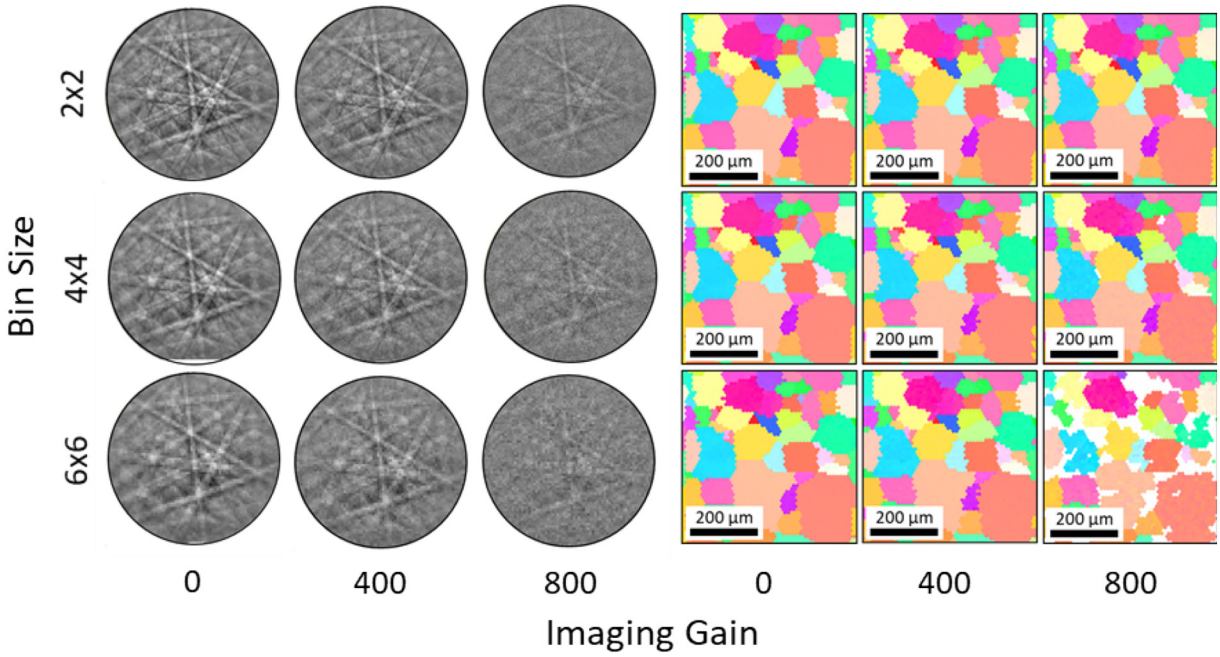

Fig. 4. The effect of bin size and imaging gain on EBSD pattern quality (left) and the subsequent effect on orientation indexing as shown by unique grain maps (right). Data is from scan of the undeformed UHP α-Ti sample.

from all samples. Overall pattern quality was excellent for all Ti specimens, but Kikuchi band contrast was especially high for undeformed UHP α-Ti. To identify optimal scanning parameters for EBSD (maximum speed while maintaining sufficient pattern quality), patterns were captured on an undeformed sample with various bin sizes (2 × 2, 4 × 4, and 6 × 6) and imaging gain (0, 400, and 800). These values were chosen because they represent a relatively broad spectrum of potential scanning parameters. For example, low binning and gain allow for high pattern quality, but scan speeds are slow due to the high exposure time associated with low gain. Conversely, high binning and high gain allows for fast scans, but sacrifices pattern quality. Single EBSD patterns collected from each of the undeformed UHP α-Ti scans (when altering bin size and gain) are shown in Fig. 4.

These scans also provided information on pattern quality from which the fraction of points indexed with a CI above 0.10 was calculated. Because patterns with a CI < 0.10 are associated with low orientation indexing accuracy [5,43–45], the ratio of points indexed with a CI < 0.10 to those > 0.10 will indicate the quality of the scan. These scans are seen in Fig. 4, which are represented as inverse pole figure (IPF) maps. Each map was post processed using a grain confidence index standardization (CIS) and grain dilation function and then thresholded to include points that only indexed with a CI > 0.10. These maps are a visual representation of the data in Table 1, which show the fraction of points indexed with a CI > 0.10.

All scans of the UHP α-Ti sample with 0 or 400 gain had over 93% of their raw patterns indexed with a CI of 0.10 or above. The scan with 2 × 2 binning and no gain also had a high percentage of raw points indexed above 0.10 CI (97%). When post processed with CIS and grain dilation, these percentages rise to 100 for all but the 4 × 4 and 6 × 6 bin sizes at 800 gain. Therefore, when accounting for scan speed, it appears 4 × 4 binning with 400 gain gives the best compromise between speed and pattern quality/indexing accuracy for undeformed UHP α-Ti within the range of tests performed. Specifically, with 4 × 4 binning and a gain of 400, we were indexing at 106 patterns per second.

Table 1
Fraction of patterns indexed with a CI > 0.10 as a function of bin size and imaging gain. Fractional values reflect post-processed data and bracketed fractional values reflect raw data. Scan taken of an undeformed UHP α-Ti sample.

		Imaging gain		
		0	400	800
Bin size	2 × 2	1.000 [0.985]	1.000 [0.975]	1.000 [0.970]
	4 × 4	1.000 [0.978]	1.000 [0.970]	0.995 [0.599]
	6 × 6	1.000 [0.968]	1.000 [0.931]	0.794 [0.118]

3.3. Microstructural characterization

Once optimal EBSD parameters were determined from smaller scans of the undeformed UHP α-Ti material, larger scans were taken on all samples using these parameters to collect bulk crystallographic orientation data at ~100 patterns per second. EBSD datasets were analyzed using the EDAX TSL Orientation Imaging Microscopy (OIM) Analysis™ software in addition to the MTEX [46] toolkit in MATLAB. All EBSD patterns were indexed as having hcp crystal structure, and although it is possible for Ti-6Al-4V to contain β-Ti, there were no bcc EBSD patterns observed in either Ti-6Al-4V scan. Each EBSD dataset underwent a CIS and grain dilation, and patterns with a CI < 0.10 were discarded. During microstructure reconstruction, grains were defined as groups of pixels numbering > 5 with > 5° of crystallographic misorientation with respect to neighboring groupings. These reconstructions allow for measurements/calculations of crystallographic texture and various twin and grain statistics to be made.

4. Results

The surface quality produced by the electropolish for the undeformed UHP α-Ti cylinder is shown in Fig. 5 compared to the surface after grinding with 600 grit SiC paper. The surface roughness was reduced significantly, and although it was not measured quantitatively in this study, Kim et al. reported a 2.341 nm surface roughness for CP Ti while using the same electrolyte solution and similar working conditions [20].

IPF maps constructed from EBSD data of the undeformed UHP α-Ti, deformed UHP α-Ti, and undeformed Ti-6Al-4V (both stress-relieved

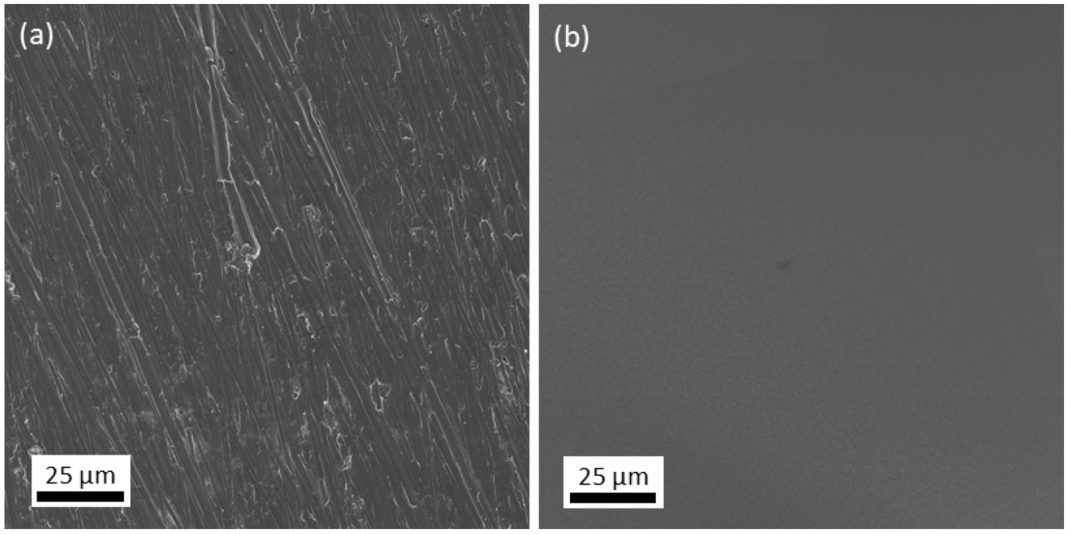

Fig. 5. Secondary electron micrographs of undeformed UHP α-Ti samples before (a) and after (b) electropolishing.

and THRM-treated) are shown in Fig. 6(a, c, e, g) and illustrate crystallographic orientation with respect to sample frame for each material. Image quality (IQ) maps in Fig. 6(b, d, f, h) allow for the spatial visualization of EBSD pattern quality and highlight the detailed microstructural features observed in the four materials. Specifically, IQ is the sum of detected peaks in the Hough transform of an EBSD pattern (the Hough transform is used for indexing a pattern) [47–49]. A perfect crystal lattice in the diffracting volume will result in the highest IQ for a given sample geometry and beam conditions. Crystallite interfaces (grain, twin, sub-grain, etc. boundaries) produce EBSD patterns with especially low IQ relative to interface-free regions. At these interfaces, backscattered electrons can originate from multiple crystallites creating superimposed EBSD patterns with slightly different orientations [47]. This lowers IQ by creating diffuse peaks in the Hough space and produces high IQ contrast at crystallite interfaces allowing for the detailed mapping of microstructures. Large grains with high IQ are seen in the undeformed UHP Ti, complex twin/grain structures are detailed in the deformed UHP Ti, and fine sub-grain structures are resolved in the stress-relieved and THRM-treated Ti-6Al-4V.

Due to differences in feature size in each material, EBSD step size was not the same when scanning each sample, as indicated in Table 2. In order to resolve the twins and sub-grain structures in the deformed UHP α-Ti and undeformed Ti-6Al-4V, respectively, smaller step-sizes than the 5 μm used for the undeformed UHP α-Ti were required. Despite the various length scales at which measurements were being made and the variety of Ti being examined (pure, alloyed, undeformed/deformed, heat-treated), once the EBSD datasets were cleaned (grain CIS and dilation), all scans had over 96% of patterns indexing with a CI $>$ 0.10 (see Table 2). The overwhelming majority of points that did not index with CI $>$ 0.10 were at grain/twin/sub-grain interfaces due to the lower indexing accuracy of low-IQ EBSD patterns. Additionally, some points in regions of high plasticity in the deformed material did not index with CI $>$ 0.10. This is due to the elevated dislocation content creating a superposition of slightly misoriented EBSD patterns, similar to what occurs at crystallite interfaces, which contributes to peak broadening in Hough space and lowers IQ [47].

5. Discussion

Ti and its alloys are usually prepared metallographically with harmful acids often at low temperatures and with high voltages. In this work, we successfully develop an electropolishing procedure for Ti with an ethanol-NaCl-ethylene glycol electrolyte solution avoiding the use of harmful acids. Importantly, the setup necessary to perform the experiment is relatively simple. High-quality scans resolving twins and sub-grain structures in the deformed UHP α-Ti and undeformed Ti-6Al-4V, respectively, are presented and discussed.

The electropolished surfaces of all Ti samples produced high-quality and high-contrast diffraction patterns when performing EBSD, from which similarly high-quality and detailed datasets were created. The electropolishing created globally flat surfaces and crystallographic orientation indexing accuracy was high. Fig. 5(b) shows no regions with abnormally high or low secondary electron signal, which indicates uniform charge distribution throughout the sample. Scratches or other sharp topographical features with edges store charge and appear bright via secondary electron imaging, which is what is seen in the unpolished micrograph in Fig. 5(a). Moreover, the IQ maps in Fig. 6 show no isolated regions of low IQ, which could indicate sample roughness at larger length scales. If there existed relief on a sample surface that was greater than the microscope's depth of focus, patterns can become out of focus and IQ and indexing accuracy can decrease. The lack of micro and macroscopic topography on electropolished surfaces, coupled with the high fraction of patterns with CI $>$ 0.10 indicates that the collection of comprehensive and accurately indexed EBSD datasets is possible. It is likely that the slight decrease in the number of patterns indexed with CI $>$ 0.10 for the deformed UHP α-Ti, stress-relieved Ti-6Al-4V, and THRM-treated Ti-6Al-4V is due to the large increase in interface density for the materials.

Additionally, the high Kikuchi band contrast observed for all samples during EBSD indicates negligible oxide formation on sample surfaces after electropolishing. Although the diffraction signal from backscattered electrons (off a metallic atomic lattice) is influenced by many factors, such as incident electron penetration angle, elemental composition, crystal structure, and defect type/density, the majority of signal originates from the top 30 nm of material when using an accelerating voltage of ~20 kV [50]. If oxide films did form, they would need to be minimal given the observed pattern quality.

Finally, electropolishing with an ethanol-NaCl-ethylene glycol electrolyte solution will produce surface finishes suitable for EBSD for other phases of pure Ti such as β-Ti, ω-Ti, and any of the metastable phases. In addition to elemental composition, the surface activity of a grain depends on its orientation, and crystal structure [51]. Variation in IQ was observed amongst grains, most notably in the undeformed UHP α-Ti sample; however, the variation was minimal and did not affect the ability to index orientations accurately. Therefore, it is assumed that crystal structure would have similarly negligible effects on orientation indexing accuracy on a Ti specimen electropolished using an ethanol-NaCl-ethylene glycol electrolyte solution.

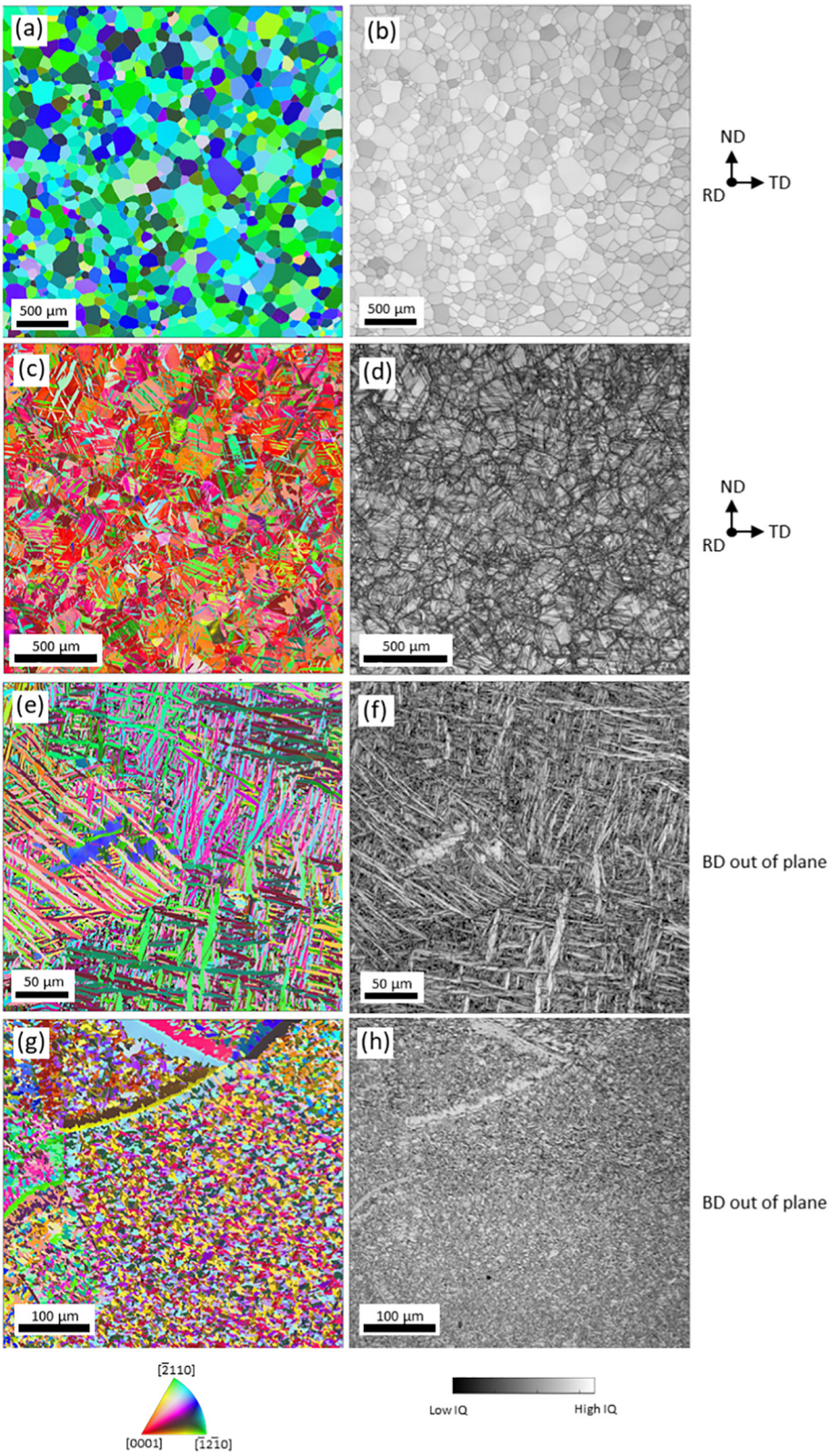

Fig. 6. IPF maps (left) and IQ maps (right) created from EBSD data for undeformed UHP α-Ti (a,b), deformed UHP α-Ti (b,c), and undeformed Ti-6Al-4V after stress-relieving (e,f), and after THRM treatment (g,h). The colors in the IPF maps represent the orientation of the sample axis with respect to the local crystal lattice frame according to the IPF color key where RD is out of plane for UHP α-Ti and BD is out of plane for Ti-6Al-4V. The contrast in the IQ maps represents EBSD pattern quality. (For interpretation of the references to color in this figure legend, the reader is referred to the web version of this article.)

Table 2
EBSD step sizes and fractions of EBSD patterns indexed with a CI > 0.10 for undeformed UHP α-Ti, deformed UHP α-Ti, stress-relieved Ti-6Al-4V, and THRM-treated Ti-6Al-4V. Fractional values were calculated from cleaned EBSD data (grain CIS and dilation) and bracketed fractional values were calculated from raw EBSD data.

	Step size (μm)	Fraction of patterns with CI > 0.10
Undeformed UHP α-Ti	5.00	1.000 [1.000]
Deformed UHP α-Ti	1.00	0.994 [0.984]
Undeformed stress-relieved Ti-6Al-4V	0.20	0.963 [0.619]
Undeformed THRM-treated Ti-6Al-4V	0.50	1.000 [0.779]

6. Conclusions

Ti and its alloys are regularly prepared metallographically with harmful acids, often at low temperatures, and with high voltages. The electropolishing of Ti and its alloys with an ethanol-NaCl-ethylene glycol electrolyte solution avoids the use of such harmful procedures. Moreover, the apparatus necessary to perform the sample preparation using the ethanol-NaCl-ethylene glycol electrolyte is relatively simple. This paper demonstrated that electropolishing pure Ti and its alloys with the described solution provides excellent surfaces from which high-quality EBSD datasets can be collected. EBSD scans performed on UHP α-Ti had excellent Kikuchi band contrast, which allowed for large areas to be scanned at fast speeds without sacrificing indexing accuracy. The electropolishing also created excellent surfaces on deformed UHP α-Ti, which featured deformation twins, and additively manufactured Ti-6Al-4V, which allowed for detailed EBSD mapping of fine microstructural features despite the increased lattice strains and Al and V alloying elements. A non-acid electrolyte solution demonstrated here to work for electropolishing of undeformed and deformed pure Ti as well as stress-relieved and THRM-treated forms of AM Ti-6Al-4V will streamline and make safer metallographic preparations of Ti and its alloys in future microstructural studies.

Declaration of competing interest

The authors declare that they have no known competing financial interests or personal relationships that could have appeared to influence the work reported in this paper.

Acknowledgements

Authors are grateful for financial support to the U.S. National Science Foundation under the CAREER grant no. CMMI-1650641. The EBSD and SEM characterization was performed in the University Instrumentation Center (UIC) at the University of New Hampshire (UNH).

Data availability

The raw/processed data required to reproduce these findings cannot be shared at this time due to technical or time limitations.

References

[1] G. Welsch, R. Boyer, E.W. Collings, Materials Properties Handbook: Titanium Alloys, ASM International, 1993.
[2] B.S. Fromm, B.L. Adams, S. Ahmadi, M. Knezevic, Grain size and orientation distributions: application to yielding of α-titanium, Acta Mater. 57 (2009) 2339–2348.
[3] G. Lütjering, J.C. Williams, Titanium, Springer, 2003.
[4] Y. Tanaka, M. Nakai, T. Akahori, M. Niinomi, Y. Tsutsumi, H. Doi, T. Hanawa, Characterization of air-formed surface oxide film on Ti-29Nb-13Ta-4.6 Zr alloy surface using XPS and AES, Corros. Sci. 50 (2008) 2111–2116.
[5] S.I. Wright, M.M. Nowell, S.P. Lindeman, P.P. Camus, M. De Graef, M.A. Jackson, Introduction and comparison of new EBSD post-processing methodologies, Ultramicroscopy 159 (2015) 81–94.
[6] X. Wu, G. Proust, M. Knezevic, S.R. Kalidindi, Elastic-plastic property closures for hexagonal close-packed polycrystalline metals using first-order bounding theories, Acta Mater. 55 (2007) 2729–2737.
[7] L.D. Zardiackas, M.J. Kraay, H.L. Freese, Titanium, Niobium, Zirconium, and Tantalum for Medical and Surgical Applications, ASTM International, 2006.
[8] M. Knezevic, R.A. Lebensohn, O. Cazacu, B. Revil-Baudard, G. Proust, S.C. Vogel, M.E. Nixon, Modeling bending of α-titanium with embedded polycrystal plasticity in implicit finite elements, Mater. Sci. Eng. A 564 (2013) 116–126.
[9] Y.S. Tian, C.Z. Chen, L.S. T., Q.H. Huo, Research progress on laser surface modification of titanium alloys, Appl. Surf. Sci. 242 (2005) 177–184.
[10] Y. Oshida, Bioscience and Bioengineering of Titanium Materials, Elsevier, 2010.
[11] N. Landry, M. Knezevic, Delineation of first-order elastic property closures for hexagonal metals using fast Fourier transforms, Materials 8 (2015) 6326–6345.
[12] T. Fast, M. Knezevic, S.R. Kalidindi, Application of microstructure sensitive design to structural components produced from hexagonal polycrystalline metals, Comput. Mater. Sci. 43 (2008) 374–383.
[13] G. Van der Voot, Metallographic preparation of titanium and its alloys, Buehler Tech-Notes 3 (1999).
[14] G. Van der Voot, W. Van Geertruyden, S. Dillon, E. Manilova, Metallographic preparation for electron backscatter diffraction, Microsc. Microanal. 12 (2006) 1610–1611.
[15] J.B. Mathieu, D. Landolt, Electropolishing of titanium in perchloric acid-acetic acid solution II. Polarization behavior and stoichiometry, J. Electrochem. Soc. 125 (1978) 1044–1049.
[16] L. Neelakantan, A. Pareek, A.W. Hassel, Electro-dissolution of 30Nb-Ti alloys in methanolic sulfuric acid-optimal conditions for electropolishing, Electrochim. Acta 56 (2011) 6678–6682.
[17] H. Zhao, J. Van Humbeeck, I. De Scheerder, Surface conditioning of nickel-titanium alloy stents for improving biocompatibility, Surf. Eng. 17 (2001) 451–458.
[18] A. Kuhn, The electropolishing of titanium and its alloys, Met. Finish. 102 (2004) 80–86.
[19] L. Sun, F.Q. Liu, S. Neo, S. Tsai, L.Y. Chen, U.S.P.a.T. Office (Ed.), (2005).
[20] D. Kim, K. Son, D. Sung, Y. Kim, W. Chung, Effect of added ethanol in ethylene glycol-NaCl electrolyte on titanium electropolishing, Corros. Sci. 98 (2015) 494–499.
[21] K. Tajima, M. Hironaka, K.K. Chen, Y. Nagamatsu, H. Kakigawa, Y. Kozono, Electropolishing of CP titanium and its alloys in an alcoholic solution-based electrolyte, Dent. Mater. J. 27 (2008) 258–265.
[22] K. Fushimi, H. Habazaki, Anodic dissolution of titanium in NaCl-containing ethylene glycol, Electrochim. Acta 53 (2008) 3371–3376.
[23] K. Fushimi, H. Kondo, H. Konno, Anodic dissolution of titanium in chloride-containing ethylene glycol solution, Electrochim. Acta 55 (2009) 258–264.
[24] S.K. Nayak, C.J. Hung, V. Sharma, S. Pamir Alpay, A.M. Dongare, W.J. Brindley, R.J. Hebert, Insight into point defects and impurities in titanium from first principles, Npj Comput. Mater. 4 (2018).
[25] P. Lejcek, Grain Boundary Segregation in Metals, Springer, 2010.
[26] ASTM E9-09, Standard Test Methods of Compression Testing of Metallic Materials at Room Temperature, ASTM International, West Conshohocken, PA, 2018.
[27] S. Ghorbanpour, M.E. Alam, N.C. Ferreri, A. Kumar, B.A. McWilliams, S.C. Vogel, J. Bicknell, I.J. Beyerlein, M. Knezevic, Experimental characterization and crystal plasticity modeling of anisotropy, tension-compression asymmetry, and texture evolution of additively manufactured Inconel 718 at room and elevated temperatures, Int. J. Plast. 125 (2020) 63–79.
[28] D.J. Savage, N.C. Ferreri, E. Vasilev, M. Knezevic, Mater. Sci. Eng. A (2020).
[29] ASTM E606/E606M-12, Standard Test Method for Strain-controlled Fatigue Testing, ASTM International, West Conshohocken, PA, 2012.
[30] S. Ghorbanpour, B.A. McWilliams, M. Knezevic, Low-cycle fatigue behavior of rolled WE43-T5 magnesium alloy, Fatigue Fract. Eng. Mater. Struct. 42 (2019) 1357–1372.
[31] J.D. Paramore, Z.Z. Fang, M. Dunstan, P. Sun, B.G. Butler, Hydrogen-enabled microstructure and fatigue strength engineering of titanium alloys, Sci. Rep. 7 (2017) 41444.
[32] S. Ghorbanpour, N.C. Ferreri, B.A. McWilliams, A.D. Kudzal, S.C. Vogel, M. Knezevic, Monotonic, cyclic, and fatigue behavior of Ti-6Al-4V fabricated via direct metal laser melting: effect of hydrogen sintering and phase transformation treatment, Int. J. Fatigue (2020).
[33] M.A. Haidekker, T.P. Brady, D. Lichlyter, E.A. Theodorakis, Effects of solvent polarity and solvent viscosity on the fluorescent properties of molecular rotors and related probes, Bioorg. Chem. 33 (2005) 415–425.
[34] D. Ballal, W.G. Chapman, Hydrophobic and hydrophilic interactions in aqueous mixtures of alcohols at a hydrophobic surface, J. Chem. Phys. 139 (2013) 114706.
[35] C.L. Yaws, H.C. Yang, To estimate vapor pressure easily, Hydrocarbon Processing, 68 1989 (USA).
[36] N.S. Peighambardoust, F. Nasirpouri, Electropolishing behaviour of pure titanium in perchloric acid-methanol-ethylene glycol mixed solution, Trans. IMF 92 (2014) 132–139.
[37] M. Rifai, H. Miyamoto, H. Fujiwara, Effects of strain energy and grain size on corrosion resistanec of ultrafine grained Fe-20% Cr steels with extremely low C and N fabricated by ECAP, Int. J. Corros. 2015 (2015).
[38] D.H. Smith, J. Bicknell, L. Jorgensen, B.M. Patterson, N.L. Cordes, I. Tsukrov, M. Knezevic, Microstructure and mechanical behavior of direct metal laser sintered Inconel alloy 718, Mater. Charact. 113 (2016) 1–9.
[39] S. Gribbin, J. Bicknell, L. Jorgensen, I. Tsukrov, M. Knezevic, Low cycle fatigue

behavior of direct metal laser sintered Inconel alloy 718, Int. J. Fatigue 93 (Part 1) (2016) 156–167.
[40] S. Gribbin, S. Ghorbanpour, N.C. Ferreri, J. Bicknell, I. Tsukrov, M. Knezevic, Role of grain structure, grain boundaries, crystallographic texture, precipitates, and porosity on fatigue behavior of Inconel 718 at room and elevated temperatures, Mater. Charact. 149 (2019) 184–197.
[41] S. Ghorbanpour, B.A. McWilliams, M. Knezevic, Effect of Hot Working on the High Cycle Fatigue Behavior of WE43 Rare Earth Magnesium Alloy, Springer International Publishing, Cham, 2019, pp. 219–225.
[42] M. Knezevic, A. Levinson, R. Harris, R.K. Mishra, R.D. Doherty, S.R. Kalidindi, Deformation twinning in AZ31: influence on strain hardening and texture evolution, Acta Mater. 58 (2010) 6230–6242.
[43] M. Knezevic, M. Zecevic, I.J. Beyerlein, J.F. Bingert, R.J. McCabe, Strain rate and temperature effects on the selection of primary and secondary slip and twinning systems in HCP Zr, Acta Mater. 88 (2015) 55–73.
[44] M. Knezevic, A. Bhattacharyya, Characterization of microstructure in Nb rods processed by rolling: effect of grooved rolling die geometry on texture uniformity, Int. J. Refract. Met. Hard Mater. 66 (2017) 44–51.
[45] M. Knezevic, J.S. Carpenter, M.L. Lovato, R.J. McCabe, Deformation behavior of the cobalt-based superalloy Haynes 25: experimental characterization and crystal plasticity modeling, Acta Mater. 63 (2014) 162–168.
[46] D. Mainprice, F. Bachmann, R. Hielscher, H. Schaeben, Descriptive Tools for the Analysis of Texture Projects With Large Datasets Using MTEX: Strength, Symmetry and Components, Geological Society of London, 2014.
[47] S.I. Wright, M.M. Nowell, EBSD image quality mapping, Microsc. Microanal. 12 (2006) 72–84.
[48] W.G. Feather, S. Ghorbanpour, D.J. Savage, M. Ardeljan, M. Jahedi, B.A. McWilliams, N. Gupta, C. Xiang, S.C. Vogel, M. Knezevic, Mechanical response, twinning, and texture evolution of WE43 magnesium-rare earth alloy as a function of strain rate: experiments and multi-level crystal plasticity modeling, Int. J. Plast. 120 (2019) 180–204.
[49] D.J. Savage, I.J. Beyerlein, N.A. Mara, S.C. Vogel, R.J. McCabe, M. Knezevic, Microstructure and texture evolution in Mg/Nb layered materials made by accumulative roll bonding, Int. J. Plast. 125 (2020) 1–26.
[50] S.F. Bordin, S. Limandri, J.M. Ranalli, G. Castellano, EBSD spatial resolution for detecting sigma phase in steels, Ultramicroscopy 171 (2016) 177–185.
[51] P.B. Sewell, C.D. Stockbridge, M. Cohen, An electron diffraction study of electropolished iron, Can. J. Chem. 37 (1959) 1813–1819.